Research Article

Influences of Hydrodynamic Forces on the Identification of the Rotor-Stator-Rubbing Fault in a Rotating Machinery

Bernard Xavier Tchomeni (iD)**, Desejo Filipeson Sozinando** (iD)**, and Alfayo Alugongo**

Vaal University of Technology, Mechanical Engineering Department, South Africa

Correspondence should be addressed to Bernard Xavier Tchomeni; bernardt@vut.ac.za

Mechanical failures of a complex machine such as rotor widely used in severe conditions often require specialized knowledge, technical expertise, and imagination to prevent its rupture. In this paper, a model for analyzing excitation of a coupled lateral-torsional vibrations of a shaft system in an inviscid fluid is proposed. The model considers the recurrent contact of the vibrating shaft to a fixed stator. The simplified mathematical model of the rotor-stator system is established based on the energy principle. The dynamic characteristics of the fluid-rotor system are studied, and the features of rub-impact are extracted numerically and validated experimentally under the effects of the unbalance and the hydrodynamic forces. The main contribution of this article is in extraction and identification of the rub features in an inviscid medium which proved to be complex by the obstruction of the fluid and required the use of appropriate signal processing tools. The results through a synchrosqueezing wavelet transform indicated that the exciting fluid force could significantly attenuate the instability and amplitude of rubbing rotor. The experimental results demonstrated that for half the first critical speed, the subharmonic $1/2 \times \Omega$ and the irregular orbit patterns provide good indices for rub detection in an inviscid fluid of the rotating shafts. Finally, it is revealed that the instantaneous frequency extraction based on wavelet synchrosqueezing is a useful tool to identify the weak and hidden peak harmonics localised in the time-frequency maps of the fluid-rotor system.

1. Introduction

Science and technology have encountered complex problems with fluid-structure interaction. The problems are strenuous to resolve because the fluid-structure interaction exhibits strong coupling, high nonlinearity, and multidisciplinary nature. In a fluid-shaft interaction problem, where one solid structure interacts with a surrounding fluid; the extraction of specific features requires an excellent comprehension of the concerned fundamental physics. The understanding can be categorised into the ensuing fields [1], a mathematical model formulation, numerical discretisation, and fluid-shaft coupling. The enlisted three categories occur sequentially. However, modelling choices at the continuous level have implications for the aptest numerical discretisation at hand [2]. The situation becomes more complicated in the fluid-shaft interaction, while the shaft is in motion. Therefore, the differential equation system must satisfy the boundary

conditions related to the fluid and structure domain simultaneously. As the shaft moves through space, the flowing sub-domain varies to suit the movement of the shaft. In this regard, the fluid motion is considered into the differential equations. For most fluid-structure interaction, problems encountered in the literature survey and analytical solutions to the model equations are widely unfeasible, whereas laboratory experiments are limited in scope. Thus, to study the fundamental physics involved in the fluid-shaft interaction with rotor-stator rubbing, numeric simulations can be a reliable alternative solution. Kadyrov et al. [3] studied the oscillations of a rigid cylinder in a cylindrical duct filled with an incompressible viscous fluid. They used theoretical mathematical analysis results for the frequency subjected to different fluid parameters. Only a few researchers have studied the vibration of rotating machinery with fault operating under the fluid domain [4, 5]. Tchomeni and Alugongo [5] identified a complex rotor vibration system, induced by the oscillation of an

unbalanced rigid rotor in a viscous fluid under the parametric excitations, namely, rub and crack. They adopted a new algorithm called wavelet denoising technique to denoise the corrupted signal in extracting the feature of the damaged rotor system in a viscous fluid medium. Their study revealed the viscous fluid forces are the sources of unwanted frequencies that initiate and expand the features of the crack along with the rotor lateral deflection shapes. Gomes and Lienhart [6] analysed the oscillation modes of self-excited flexible structure in a uniform flow of different Reynolds numbers. The investigation was performed in different fluid properties such as an inviscid and highly viscous fluid, considering three different geometry structures. The results were definite and showed the characteristic of the structure motion in the sequence of oscillation modes as a function of the structure characteristic of the flow. As the demand for high speed in modern rotating machinery and high efficiency is increasing, inclusively, the contact between the rotating rotors and fixed stators is becoming periodic due to the reduction of the clearance. Gearing towards this result, the rubbing impact with the interaction between rub-impact and oil-film forces in a machine has become one of the most common damaging malfunctions of rotating machinery [7]. Investigation on the mechanism of the rub-impact phenomenon and its dynamic characteristics attracts many researchers and scientists to improve the current diagnosis of rotor systems. Popprath and Ecker [8] presented a Jeffcott rotor model with intermittent contact with a stator interacting with the rotor model via nonlinear contact forces. The submodel of the stator was displayed as an additional vibratory system. Bachschmid et al. [9] studied the thermally induced spiral vibrations using a fully assembled machine model (rotor, bearings, and foundation) and implemented a sophisticated thermal and contact model with one-dimensional finite beams and a three-dimensional model for temperature distribution analysis. Banakh and Nikiforov [10] examined vibroimpact interaction between the rotor and floating sealing ring where hydrodynamic forces in the clearance between the rotor and the ring, as well as dry friction between the ring and the casing, were considered. Above all, owing to the cited works, no empirical results were given. Presently, a few researchers are still devoted to investigate experimentally the dynamic stability of the rotor filled with liquid. Zhu et al. [11] made the experimental analysis on the dynamic characteristics of an overhung rigid centrifuge rotor partially filled with fluid. The research chiefly focused on the influences of viscous fluid-fill ratio on rotor whirl frequency, the range of the unstable region, and the rotor unbalance. Hengstler [12] provided experimental results for a submerged and confined disc, with rotating fluid on the lower surface. In both cases, the liquid was rotating with respect to the disc, but the disc was standing. Presas et al. in [13] studied a disc that is forced to rotate inside a tank full of water. They performed a disc test rig which consists of a rotating disc structure excited with a piezoelectric patch from the rotating frame and submerged in heavy fluids both in rotating and stationary frames. They concluded that the rotating structures submerged in heavy fluids are different from rotating systems in the air, including the transmission

from the rotating frame to the stationary frame. Since the unbalance and rubbing faults are widely observed in the rotor system, distinguishing them is becoming more attractive.

In this paper, the dynamic model of a fluid-rotor interaction system, together with single-point unbalanced rotor-stator rub-impact, is established. The equations governing the coupled fluid rotor system are derived using the Lagrange formulation and numerically solved to illustrate the rub-impact fault between higher speed shaft rotation and fixed stator. Strictly narrowing, the paper mainly emphasised the oscillated feature of nonlinear rotor-stator rubbing impact and the induced IF obtained by NWSST at the contact point. Considering these outcomes, the paper presents a test rig to analyse the dynamic vibration, a rotating system in a container filled with inviscid fluid (water). The overleaf headings of the present paper are organised as follows: in Section 2, the equations governing the coupled fluid rotor system are derived, and the single-point rub-normal impact force and tangential friction force are expressed; in Section 3, an approach of calculating the hydrodynamic effects of the fluid is derived from the fluid-shaft coupling model, based on which the highly oscillated feature of NWSST and IF is theoretically obtained, the definition of IF is provided, and the methods of NWSST are introduced briefly; in Section 4, the highly oscillated feature of the signal induced by rubbing faults in an inviscid fluid is extracted from the dynamic responses by utilizing the NWSST method in various scenarios; in Section 5, an experiment is conducted on a Rotor Kit 4 rotor test rig to validate the effectiveness of applying the time-frequency method to extract the features of the rotor-stator system in a fluid medium. The influences of dynamic parameters, i.e., rub clearance, unbalance, and fluid density on the oscillated features of IF, are also investigated; and finally, considering the discussed preceding sections, definite conclusions are drawn in Section 6.

2. Mathematical Model of the Interconnected Shafts

Figure 1(a) represents the schematic overview of a flexible shaft-disc partially submerged in an inviscid fluid. The model was used for the analysis of a fluid-rotor-stator system driven by an electrical motor. A massless elastic shaft with a disc, supported by bearings having asymmetrical stiffness and damping, is partially submerged in the container filled by an inviscid fluid. The frames of reference of the rotor system, with the origin O, put at the centre of the shaft-disc, is also shown in Figure 1(b). The inertia coordinate axes O - X, Y, and Z are chosen such that O - Z lies along the rotor shaft. An excitation simulating rubbing forces is included in the model and generated a nonlinear system equation. The equations of motion of a submerged unbalanced rotor-stator system presented in Figure 1 are established based on the energy principle and Lagrangian techniques. To develop the equation of motion for the rotor-stator system, it is assumed that the heats were generated during rub-impact; the internal friction other than rotor to the stator and the gravitational forces are neglected. The rotor system accounts only for one angular displacement of the shaft-disc θ and two orthogonal lateral
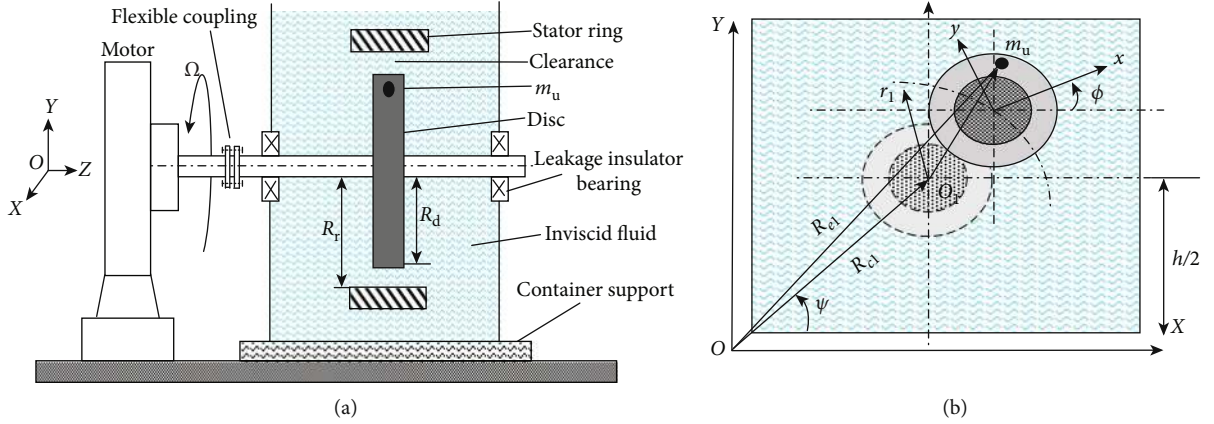
FIGURE 1: (a) Schematic of the fluid-rotor-stator system. (b) View of a disc in fixed coordinates.

defections of the shaft-disc in the inertia coordinate centre (O, X, Y). The deformed coordinate systems used are displayed in Figure 1(b), where x, y is a shaft coordinate system with the disc which exhibits all its motions. The attached unbalance mass, m_u, is located by the eccentricity vector e with respect to the disc body coordinate system x, y.

2.1. Expression of the Kinetic Energy. The system kinetic energy is the sum of the lateral and the rotational kinetic energy mass unbalance and motor system, which can be expressed as

$$G_D = \frac{1}{2}(J_1 + J_2)\dot{\theta}^2 + \frac{1}{2}M\left(\dot{X}^2 + \dot{Y}^2\right) + \frac{1}{2}m_u \dot{R}_e^T \dot{R}_e, \quad (1)$$

where individual inertia J_2 is the motor mass inertia; J_1 the shaft-disc mass inertia and $\dot{R}_e$ is the velocity vectors of mass m_u which can be expressed in the inertial reference frame using the rotational transformation matrices as follows [5]:

$$\dot{R}_e = \begin{Bmatrix} \dot{X} - \dot{\theta}e_y \cos\theta - \dot{\theta}e_y \sin\theta \\ \dot{Y} + \dot{\theta}e_x \cos\theta - \dot{\theta}e_y \sin\theta \end{Bmatrix}, \quad (2a)$$

$$\frac{1}{2}m_u \dot{R}_e^T \dot{R}_e = \frac{1}{2}m_u\left[e^2\dot{\theta}^2 + \left(\dot{X}^2 + \dot{Y}^2\right) - 2\dot{X}\dot{\theta}\left(e_x \sin\theta + e_y \cos\theta\right) + 2\dot{Y}\dot{\theta}\left(e_x \cos\theta - e_y \sin\theta\right)\right], \quad (2b)$$

where e_x and e_y are components of eccentricity e projected in x, y. Substituting Equation (2) into Equation (1), the final the kinetic energy expression becomes

$$G_D = \frac{1}{2}(J_1 + J_2)\dot{\theta}^2 + \frac{1}{2}(M + m_u)\left(\dot{X}^2 + \dot{Y}^2\right) + \frac{1}{2}m_u e^2\dot{\theta}^2 - m_u\dot{X}\dot{\theta}\left(e_x \sin\theta + e_y \cos\theta\right) + m_u\dot{Y}\dot{\theta}\left(e_x \cos\theta - e_y \sin\theta\right). \quad (3)$$

2.2. Expression of the Potential and Dissipative Energy. The potential energy of shaft comprising strain energy of bending is expressed as

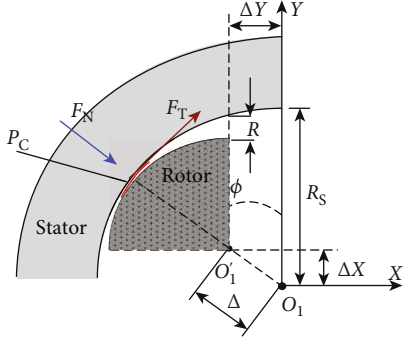$$V_P = \frac{1}{2}K_{XX}X^2 + \frac{1}{2}K_{YY}Y^2, \quad (4)$$

FIGURE 2: Forces acting on the rotor-stator rub with clearance.

where K_{XX} and K_{YY} are the stiffness coefficients related to the system degrees of freedom. For a damping rotor system, Rayleigh's dissipation function is given by

$$V_R = \frac{1}{2} C_{XX} \dot{X}^2 + \frac{1}{2} C_{YY} \dot{Y}^2, \tag{5}$$

where C_{XX} and C_{YY} are the respective damping coefficients.

2.3. Single-Point Rotor-Stator Contact Model. In this section, the interaction between a rotor and the fixed casing will be studied in more detail. Contact stress theory is used for the contact force model. The contact force between the rotor and stator is modelled as a linear damper and spring model. The rub forces consist of the radial contact force (blue arrow in Figure 2) and the tangential friction force (brown arrow in Figure 2). This model will allow dynamic studies for a rotating structure and will validate the physical rotor model.

The instantaneous location of the shaft-disc in contact with the stator at P_c usually occurs once the contact stiffness between rotor and stator is so significant that the rotor bounces off the stator by the impact forces. Suppose the inertia of the stator is neglected. In that case, the model considers the hard surface of the disc and the stator and its elastic properties are summarised in the stiffness and damping matrices K_S and D_S. The conventional spring approach in [14] is adopted. The friction force is constituted with the contact spring force F_S, the damping F_T forces F_D, and the dry friction forces F_F when $R \geq \Delta$ written as follows:

$$\begin{aligned} F_S(\delta) &= K_S(R - \Delta), \\ F_D(v_\delta) &= D_S v_\delta, \\ F_F(\delta) &= -\lambda K_S(R - \Delta), \end{aligned} \tag{6a}$$

where K_s, D_S, λ, and Δ are the stator radial stiffness parameter, the linear contact damping, the sliding friction coefficient, and the radial clearance between the disc and the stator, respectively. δ is the radial response of the shaft's geometrical centre and $v_\delta = \dot{\delta}$ is the relative velocity obtained by differentiating Equation (6b). From the geometry of Figure 3, the value of δ and $\dot{\delta}$ at an arbitrary point P_c, is determined as follows:

$$\delta = R - \Delta,$$

$$R = \sqrt{(X_r - X_s)^2 + (Y_r - Y_s)^2},$$

$$\dot{\delta} = \frac{d\delta}{dt} = \frac{(X_r - X_s)(\dot{X}_r - \dot{X}_s) + (Y_r - Y_s)(\dot{Y}_r - \dot{Y}_s)}{\sqrt{(X_r - X_s)^2 + (Y_r - Y_s)^2}}, \tag{6b}$$

where the stator coordinate is defined by X_s, Y_s. As energy dissipation takes place between the two rigid bodies' contact, the contact is modelling such as a simple spring-damper model, where a linear spring-damper element represents the contact force. When rub-impact occurs, the rub-impact force is separated into an elastic and dissipative force expressed as

$$F_N = K_S . \delta^n + D_S \dot{\delta}. \tag{6c}$$

For the two circular contacts of the disc and the annular stator, the exponent n can be set to 1.5, which makes Hertz's model nonlinear. The stiffness coefficient is expressed, respectively, in the function of the rotor and stator radius R_r and R_s, and of the material properties of the disc and casing stator. One has

$$K_S = \frac{4}{3(\sigma_r + \sigma_s)} \sqrt{\frac{R_r R_s}{R_r + R_s}}, \tag{7}$$

where $\sigma_r = (1 - v_r^2)/E_r$, $\sigma_s = (1 - v_s^2)/E_s$, and σ_r and σ_s represent, respectively, Poisson's ratio of the rotor and stator. E_r and E_s are the elastic modulus of the rotor and stator, respectively. The contact damping $D_S = \kappa \dot{\delta}^n$ is a function of the rubbing restitution coefficient ε and the initial impact velocity $\dot{\delta}^{(-)}$ given as follows:

$$\kappa = \frac{3K_S(1 - \varepsilon^2)}{4\dot{\delta}^{(-)}}. \tag{8a}$$

The regular contact force is finally written as

$$F_N = K_S \delta^n \left[1 + \frac{3(1 - \varepsilon^2)\dot{\delta}}{4\dot{\delta}^{(-)}} \right]. \tag{8b}$$

The energy dissipation due to the impact in each direction can be expressed when rub occurs, i.e., $\delta \geq \Delta$; thus, the rub forces F_X and F_Y in Equation (6) can be rewritten in the X and Y directions as

$$\begin{Bmatrix} F_X = -F_N \cos\phi + F_T \sin\phi \\ F_Y = -F_N \sin\phi - F_T \cos\phi \end{Bmatrix} \Leftrightarrow \begin{Bmatrix} F_X \\ F_Y \end{Bmatrix} = F_N \begin{pmatrix} -1 & \lambda \\ -\lambda & -1 \end{pmatrix} \begin{Bmatrix} \cos\phi \\ \sin\phi \end{Bmatrix}, \tag{9a}$$
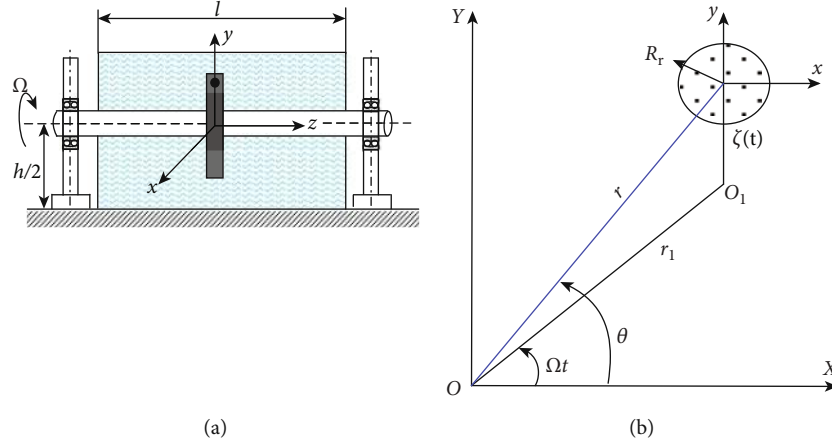
(a)

(b)

Figure 3: Schematic of a submerged rotor in the inviscid fluid (a) rotor under lateral excitation and (b) fluid profile.

and the Coulomb friction torque is stated as

$$T_\theta(\delta) = -K_S R_D \delta \lambda \left(1 - \frac{\Delta}{\delta}\right),\qquad(9b)$$

where R_D is the disc's radius, $X = \delta \cos \phi$, and $Y = \delta \sin \phi$. After the rub-impact, the rotor responds with complex transient lateral and torsional motions.

3. Hydrodynamic Forces under Lateral Excitation Force

In this section, the hydrodynamic forces acting on an upright rectangular tank are derived along the X- and Y-axes. For simplification, the following assumptions of the system are made: (1) the container is rigid and impermeable; (2) under shaft excitation, the inviscid incompressible and initially irrotational fluid motion is at low Reynolds number caused by small-amplitude vibration motion of the rotor system; (3) the laminar-turbulent transition process of the inviscid fluid on the rotating shaft-disc is not taken into consideration; and (4) for abrupt changes of cross section, the radius of the disc is closer to the shaft radius ($r_{shaft} \approx r_{disc}$). The fluid does not participate in the shaft motion since it is assumed to be inviscid. The Euler equations are applied to estimate the mass of the fluid participating in the rotor motion. Based on the two-dimensional analysis of fluid motion in a rectangular container of depth h and width l as shown in Figure 3. The derivation of the hydrodynamic forces acting around the rotating shaft under sinusoidal lateral excitation is established herein as discussed in [15]. The rise of a dynamic unbalance in which centre of mass is then sent off the centerline of the shaft, resulting in harmonic excitation in X- and Y-axes by

$$\begin{aligned} X(t) &= X_0 \cos \Omega t, \\ Y(t) &= Y_0 \sin \Omega t, \end{aligned}\qquad(10)$$

where $X_0 Y_0$ are the excitation amplitude and Ω is a cyclical frequency in cycles per unit of time much lower than its

fundamental frequency ($\omega \ggg \Omega$) so that the liquid oscillates at exactly the excitation frequency.

Under the assumption that the amplitudes of excitation and fluid response are small for irrotational, inviscid, and incompressible flow motion, the governing equation for the fluid velocity potential function $\tilde{\Phi}$ results in Laplace's equation as [15]

$$\nabla^2 \tilde{\Phi} = 0, \quad \text{inside the fluid domain},\qquad(11a)$$

$$\nabla^2 = \frac{\partial^2}{\partial r^2} + \frac{1}{r}\frac{\partial}{\partial r} + \frac{1}{r^2}\frac{\partial^2}{\partial \theta^2},\qquad(11b)$$

where $\tilde{\Phi} = \tilde{\Phi}(r, \theta, t)$ is associated with the perturbations to the flow and depends on the Eulerian coordinates and the time, the presence of the rotor is immersed in a finite extending fluid region for $r = l$ (i.e., the container width is taken as l), and the boundary conditions at the container solid boundaries are

$$\begin{aligned} \left.\frac{\partial \tilde{\Phi}}{\partial r}\right|_{r=l} &= 0, \\ \left.\frac{\partial \tilde{\Phi}}{\partial z}\right|_{z=h} &= 0, \\ \left.\frac{\partial \tilde{\Phi}}{\partial \theta}\right|_{\theta=0,\pi/2} &= 0, \end{aligned}\qquad(12)$$

The combined free-surface condition which is obtained from the kinematic condition is

$$g\eta - \frac{\partial \tilde{\Phi}}{\partial t} + \ddot{x} r \cos \theta = 0, \quad \text{at } z = \eta(r, \theta, t),\qquad(13)$$

and the vertical velocity of a fluid particle located on the free surface $z = \eta(r, \theta, t)$ should be equated to the vertical velocity of the free surface itself to give the linearised dynamic free-surface condition:

$$-\frac{\partial \tilde{\Phi}}{\partial z} = \frac{\partial \eta}{\partial t}, \quad \text{at } z = \eta(r, \theta, t), \tag{14}$$

where $\eta(r, \theta, t)$ is the fluid surface elevation measured from the undisturbed free surface. Differentiating once the dynamic conditions (13) with respect to time and kinematic free-surface conditions (14) gives

$$\frac{\partial^2 \tilde{\Phi}}{\partial t^2} + g \frac{\partial \tilde{\Phi}}{\partial z} = \ddot{x} r \cos \theta. \tag{15}$$

The function $\tilde{\Phi}$ satisfies the following conditions on the fluid boundary: $\partial \tilde{\Phi}/\partial \eta = 0$, at the container walls, and $\partial \tilde{\Phi}/\partial \eta = -\dot{\eta}$, at the free surface. $\dot{\eta}(r, \theta, t)$ is the vertical velocity of the free surface. The typical solution of the continuity Equation (11) subject to boundary conditions (12) can be expressed as

$$\tilde{\Phi}(r, \theta, z, t) = \sum_{n=1}^{\infty} \left[C_{1n}(t) \cos \theta + D_{1n}(t) \sin \theta \right] J_1(k_{1n}r) \frac{\cos h(k_{1n}(z+h))}{\cos h(k_{1n}h)} \Big], \tag{16}$$

where the function C_{1n} and D_{1n} are time-dependent to be determined from the free-surface initial conditions (15), $J_1(.)$ is the Bessel function of the first kind of order 1, and $k_{1n} = \xi_{1n}/l$ are roots of $\partial J_1(k_{1n}r)/\partial r|_{r=l} = 0$. It is assumed that $r(t)$ is a weak function of time, in order words, $r(t) \simeq r_1 + \zeta(t) \approx r_1$, where $\zeta(t)$ is a low-order perturbation function and r is a Fourier-Bessel series expansion given in the form as

$$r = \sum_{n=1}^{\infty} F_n J_1(k_{1n}r), \tag{17}$$

where $F_n = 2l/(k_{1n}^2 l - 1)J_1(k_{1n}l)$.

Introducing Equations (10) and (11) into the free-surface condition (14) yields to

$$\sum_{n=1}^{\infty} \left[\ddot{C}_{1n}(t) + \omega_{1n}^2 C_{1n}(t) - \frac{\ddot{x}F_n}{\cos h(k_{1n}h)} \right] J_1(k_{1n}r) \cos \theta$$
$$+ \left[\ddot{D}_{1n}(t) + \omega_{1n}^2 D_{1n}(t) \right] J_1(k_{1n}r) \sin \theta = 0, \tag{18a}$$

where the natural frequency of the liquid free surface in a rigid rectangular tank ω_{1n} can be obtained if the functions C_{1n} and D_{1n} are expressed as harmonics function, $\sin \omega_{1n}t$. By substituting Equation (16) into homogeneous Equation (17), the natural frequencies expression is derived and expressed as

$$\frac{(\omega_{1n}^2 \cos h((h+z)k_{1n}) - g \sin h((h+z)k_{1n})) \sin (\omega_{1n}t)(\cos \theta + \sin \theta)}{\cos h(hk_{1n})} = 0. \tag{18b}$$

The corresponding natural frequencies are given by

$$\omega_{1n}^2 = \frac{g\xi_{1n} \tan h(\xi_{1n}h/l)}{l}, \tag{18c}$$

where ξ_{1n} are the roots of $\partial J_1(k_{1n}r)/\partial r|_{r=l} = 0$ and expression (18a) is satisfied if the functions C_{1n} and D_{1n} satisfy the following differential equations:

$$\ddot{C}_{1n}(t) + \omega_{1n}^2 C_{1n}(t) = \frac{\ddot{x}F_n}{\cos h(k_{1n}h)}, \tag{19a}$$

$$\ddot{D}_{1n}(t) + \omega_{1n}^2 D_{1n}(t) = 0. \tag{19b}$$

The steady-state solutions of Equations (19a) and (19b) are

$$C_{1n}(t) = -\frac{\Omega^3}{(\omega_{1n}^2 - \Omega^2)} \frac{X_0 F_n}{\cosh (\xi_{1n}h/l)} \cos \Omega t, \tag{20a}$$

$$D_{1n}(t) = 0. \tag{20b}$$

By substituting Equations (20a) and (20b) into expression (16), the velocity potential function is given by

$$\tilde{\Phi} = -X_0 \Omega \cos \theta \cos \Omega t \sum_{n=1}^{\infty} \left[\frac{2l}{(\xi_{1n}^2 - 1)} \frac{\Omega^2}{(\omega_{1n}^2 - \Omega^2)} \frac{J_1(\xi_{1n}r/l)}{J_1(\xi_{1n})} \frac{\cos h(\xi_{1n}(z+h)/l)}{\cos h(\xi_{1n}h/l)} \right]. \tag{21}$$

The total potential function is obtained by summing the fluid perturbed function $\tilde{\Phi}$ and the tank potential

function $\Phi_0 = -X_0 \Omega \cos \theta \cos \Omega t$, $(\Phi = \tilde{\Phi} + \Phi_0)$ and expressed as

$$\tilde{\Phi} = -X_0 \Omega \cos \theta \cos \Omega t \times \left\{ r + \sum_{n=1}^{\infty} \left[\frac{2l}{\left(\xi_{1n}^2 - 1\right)} \frac{\Omega^2}{\left(\omega_{1n}^2 - \Omega^2\right)} \frac{J_1(\xi_{1n}r/l)}{J_1(\xi_{1n})} \frac{\cos h(\xi_{1n}(z+h)/l)}{\cos h(\xi_{1n}h/l)} \right] \right\}. \tag{22}$$

The hydrodynamic force is obtained by integrating the pressure distribution over the rectangular tank walls and bottom. Since the fluid is inviscid, there is no shear, and the hydrodynamic pressure at any point inside the fluid domain (by neglecting the hydrostatic pressure, $\rho g z$) may be determined from the pressure equation as follows:

$$p = \rho \frac{\partial \tilde{\Phi}}{\partial t} = \rho \Phi_0 \Omega \left\{ r + \sum_{n=1}^{\infty} \left[\frac{2l}{\left(\xi_{1n}^2 - 1\right)} \frac{\Omega^2}{\left(\omega_{1n}^2 - \Omega^2\right)} \frac{J_1(\xi_{1n}r/l)}{J_1(\xi_{1n})} \frac{\cos h(\xi_{1n}(z+h)/l)}{\cos h(\xi_{1n}h/l)} \right] \right\}. \tag{23}$$

The pressure distribution on the wall occurs at $r = h$, on the disc at $z = -h, \theta = 0$, and $\Omega t = \pi/2$. It is given by the expression

$$\frac{p_w}{\rho g l (X_0/l)} = \frac{\Omega^2 l}{g} \left\{ 1 + \sum_{n=1}^{\infty} \left[\frac{2}{\left(\xi_{1n}^2 - 1\right)} \frac{\Omega^2 l/\xi_{1n}g \tan h(\xi_{1n}h/l)}{\left(1 - \Omega^2 l/\xi_{1n}g \tan h(\xi_{1n}h/l)\right)} \frac{\cos h(\xi_{1n}(z+h)/l)}{\cos h(\xi_{1n}h/l)} \right] \right\}. \tag{24}$$

Similarly, the pressure distribution on the bottom at $z = -h, \theta = 0$, and $\Omega t = \pi/2$ is

$$\frac{p_b}{\rho g l (X_0/l)} = \frac{\Omega^2 l}{g} \left\{ \frac{r}{l} + \sum_{n=1}^{\infty} \left[\frac{2}{\left(\xi_{1n}^2 - 1\right)} \frac{\Omega^2 l/\xi_{1n}g \tan h(\xi_{1n}h/l)}{\left(1 - \Omega^2 l/\xi_{1n}g \tan h(\xi_{1n}h/l)\right) \cos h(\xi_{1n}h/l)} \frac{J_1(\xi_{1n}r/l)}{J_1(\xi_{1n})} \right] \right\}. \tag{25}$$

The integer n is the circumferential mode representing the rotor deformation. Consider the oscillation for the fundamental mode $m = n = 1$ such that the net hydrodynamic force components acting on the tank wall and bottom are obtained by integrating the pressure over the corresponding area of the boundary. Resolving along $\theta = 0$, the total hydrodynamic force exerted by the fluid on the vertical shaft along the fixed coordinate X- and Y-axes is

$$F_{XY} = \int_0^{2\pi} \int_{-h}^0 p \cos\theta l\, d\theta\, dz \Rightarrow F_{XY} = m_f X_0 \Omega^2 \sin\Omega t \times \left\{ 1 + \frac{2l}{\left(\xi_{1n}^2 - 1\right)} \frac{\Omega^2}{\left(\omega_{1n}^2 - \Omega^2\right)} \frac{\tan h(\xi_{1n}h/l)}{\xi_{1n}h} \right\}, \tag{26}$$

where $m_f = \rho\pi h l^2$ is the total mass of the fluid. The full hydrodynamic force on the container wall $r = l$ and at any point on the bottom $z = -h/2$, respectively, is

$$F_Z = \int_{\theta=0}^{2\pi} \int_{-h}^0 p \sin\theta l\, d\theta\, dz = 0,$$
$$F_b = \int_{\theta=0}^{2\pi} \int_{r=0}^l p r\, d\theta\, dr = 0. \tag{27}$$

These results indicate that there is a net force exerted along the direction of excitation as given by relation (26). In the perpendicular direction, the pressure distribution is symmetrical about the tank such that the integration over it

vanishes. The pressure at the tank bottom produces no forces in the direction of excitation. It is noted that the introduction of concepts of resistance forces for such liquid-level systems enables one to describe their dynamic characteristics in simple forms. Therefore, consider the coordinates of the shaft centre along the X and Y-axes:

$$X(t) = l \cos\Omega t,$$
$$Y(t) = l \sin\Omega t. \tag{28}$$

The hydrodynamic force generated by the rotor motion can be rewritten into

$$F_{XX} = -M_{fl} \frac{d^2 Y}{dt^2}, \quad \text{where } M_{fl} = m_f X_0 \times \left\{ \frac{1}{l} + \frac{2}{\left(\xi_{1n}^2 - 1\right)} \frac{\Omega^2}{\left(\omega^2 - \Omega^2\right)} \frac{\tan h(\xi_{1n}h/l)}{\xi_{1n}h} \right\}. \tag{29}$$

For inviscid and incompressible flow, the added mass of fluid is coupled to the inertial force of the shaft as

$$m_{XX} = m_{YY} = M + m_u + M_{fl}. \tag{30}$$

The governing equation of the fluid-rotor interaction is acquired by expressing a general dynamic equation of a rotor

system using generalised coordinates. Upon substituting Equations (3)–(5) into Lagrange's equations, introducing the fluid forces into the system and performing some suitable manipulations, thus, the final equation of the system is represented as a three-degree-of-freedom torsional and lateral nonlinear system written as

$$\begin{bmatrix} J_1 + J_2 + m_u e^2 & -em_u \sin 2\theta & em_u \cos 2\theta \\ -em_u \sin 2\theta & M + m_u + M_{fl} & 0 \\ em_u \cos 2\theta & 0 & M + m_u + M_{fl} \end{bmatrix} \begin{Bmatrix} \ddot{\theta} \\ \ddot{X} \\ \ddot{Y} \end{Bmatrix} + \begin{bmatrix} 0 & 0 & 0 \\ 0 & C_{XX} & C_{XY} \\ 0 & C_{YX} & C_{YY} \end{bmatrix} \begin{Bmatrix} \dot{\theta} \\ \dot{X} \\ \dot{Y} \end{Bmatrix} + \begin{bmatrix} 0 & 0 & 0 \\ 0 & K_0 & K_{XY} \\ 0 & K_{YX} & K_0 \end{bmatrix} \begin{Bmatrix} \theta \\ X \\ Y \end{Bmatrix} + \begin{Bmatrix} 2m_u e \cos(2\theta)\dot{\theta}\dot{X} + 2m_u e \sin(2\theta)\dot{\theta}\dot{Y} \\ 2m_u e \cos(2\theta)\dot{\theta}^2 \\ 2m_u e \sin(2\theta)\dot{\theta}^2 \end{Bmatrix} = \begin{Bmatrix} T_\theta \\ F_X \\ F_Y \end{Bmatrix}. \tag{31}$$

The first matrix of Equation (31) represents the system inertia mass matrix which is influenced by the unbalance and the rotational degree of freedom. The second and third matrices are, respectively, the linear damping and stiffness

matrices. The first term on the right hand represents the non-linear Carioles vector affected by the velocity vector of the rotational degree of freedom, the rotor lateral degrees of freedom, X and Y, and the mass unbalance. It is noted that the

effects of crosscoupling of the stiffness and damping coefficients are zero; therefore,

$$C_{XY} = C_{YX} = K_{XY} = K_{YX} = 0. \quad (32)$$

3.1. Brief Presentation of Nonlinear Wavelet Synchrosqueezing Algorithm. Features extracted from the vibration response of the multifault rotor-stator system comprise complex nonstationary signal containing essential information of the system health condition. Since the signal of the vibration system generated by the rub-impact presents nonlinearity, discretisation of such a system inside a fluid becomes more complex using the classical method. To assess the system condition and improve the fault diagnosis, an IF obtained by NWSST [16] is introduced to extract the hidden in the weak feature of the signals. A brief overview of the theory underlying the proposed technique is given here.

As a singular reallocation method, synchrosqueezing is based on wavelet transform (WT) and is aimed at refining the WT coefficient $W(t, \omega)$ by transferring its value to the different points (t', ω'); therefore, it is necessary to introduce the WT first. For a chosen mother wavelet function, the CWT of the Hilbert transform signal $z_n(t)$ is defined by

$$W_x(a, b) = \int_{-\infty}^{+\infty} z_n(t) \frac{1}{\sqrt{a}} \overline{\psi\left(\frac{t-b}{a}\right)} dt, \quad (33)$$

where a is the scale factor, b is the dilation factor, and $\overline{\psi((t-b)/a)}$ represents the complex conjugate of $\psi((t-b)/a)$. The mapping between scale factor a and signal frequency ω makes visualising wavelet coefficients in the time-frequency plane easier. The Fourier transform $\widehat{\psi}(\xi)$ of the decayed mother wave function ψ is approximately equal to zero in the negative frequencies: $\widehat{\psi}(\xi) = 0$ for $\xi < 0$ and is concentrated around $a = \omega_0/\omega$. Its IF is preliminarily evaluated by taking derivatives of wavelet coefficients. The formula of its computation is shown as follows:

$$\omega_x(a, b) = \begin{cases} -j\partial_b W_x(a, b)/W_x(a, b) & \text{if } |W_x(a, b)| > 0, \\ \infty & \text{if } |W_x(a, b)| < 0, \end{cases} \quad (34)$$

with the map built by Equation (34); in the next synchrosqueezing step, the frequency variable ω and scale factor a were computed only at discrete points a_i, with $(\Delta a)_i = a_i - a_{i-1}$, and its synchrosqueezing value was similarly determined only at the centers ω_s of closed intervals $[\omega_s - 1/2\Delta\omega, \omega_s + 1/2\Delta\omega]$, with $\Delta\omega = \omega_s - \omega_{s-1}$. By summing these different contributions, synchrosqueezing wavelet transform of $x(t)$ is obtained as

$$T_x(\omega_s, b) = \int_{A(b)} W_x(a, b) a^{-3/2} \delta(\omega(a, b) - \omega) da. \quad (35)$$

Some differences exist between synchrosqueezing and time-frequency representation technique similar to CWT distribution. NWSST is invertible and allows individual recon-struction of its components. So, the IF of the original signal $z_n(b)$ can be reconstructed by performing an inverse transform to $T_x(\omega_s, b)$ as shown in [17]. After the completion of the signal conversion frequency, the next step is to use the time-frequency of signal processing to extract the fault information contained in the time-frequency plot.

3.2. Model Properties. The damping factor will depend on the liquid height and tank width for rectangular cross section when the above expression $\omega_n^2 = g\xi_{mn}/l \tan h(\xi_{mn}h/l)$ of the liquid free surface approaches a constant value for $h/l \geq 2$, $\tan h(\xi_{mn}h/l) \approx 1$ and for the first asymmetric mode in a circular rotor $\xi = 1.841$ and $\omega_{1n}^2 = g\xi_{1n}/l$, where l is the tank width. In order to simulate the rubbing fault in the system, the estimated clearance is $\delta = 2.5 \times 10^{-5} m$, and the rubbing restitution coefficient as calculated in [14] is allowed. All relevant data of physical parameters of a typical disc-shaft-fluid used is displayed in Table 1.

4. Numerical Simulation Results and Discussions

The nonlinear dynamics of the fluid coupled to a rotor-stator with transient masses is simulated in this section. Based on Equation (31), the dynamic responses are obtained by the Runge-Kutta method. The reaction of the rotor system is presented through the changes in orbit, the lateral deflection of the shaft, the frequency spectrum, and the synchrosqueezing spectrum. At first, friction and fluid will be neglected, and the dynamic equilibrium positions will then be sought. Finally, the friction and fluid will be considered, and the dynamic behaviour of the resulting system is highlighted.

5. Results and Discussion

The response of the orbits is shown in Figure 4. The orbit of the unbalanced shaft rotor (even with fluid) is formed of n interwoven circular loops in shape (Figures 4(a) and 4(b)). Monitoring the orbits can be very useful in detecting the presence of distortion due to rubbing. In the presence of an inviscid fluid, a weak rub-impact is created, which partly distorted ellipses of shaft centre orbits, as shown in Figure 4(d) compared to Figure 4(c).

The frequency spectrum of the response in Figure 5 makes it possible to verify that a single vibration develops at a frequency corresponding to that of the coupling of the shaft at the resonance. It may be noticed that the harmonics of 1× order (53.38 Hz) exists in each dynamic response. The higher frequency 1× get excited as unbalance takes place. The FFT spectral plot shows that subharmonic resonance with a noise peak at 1/2× and 1/4× of the critical speed can be observed in the unbalanced-rub-impact system in Figure 5(c). Inside the fluid, weak subharmonic resonance at 1/2×, of the critical bending speed, can be observed in the rubbing rotor (Figure 5(d)). It should be noted that the damping characteristics of the fluid significantly modify the critical harmonic peak response of the rotor, dropping its critical speed by up to 25%. This is also confirmed in Figure 6(b) where the embraced part by red dashed line

TABLE 1: Parameters of the rotor-stator system for the simulations.

| Shaft parameters	Value and units	Bearing stiffness	Value and units
Length of the shaft	780 mm	Shaft stiffness (K_0)	5.35×10^5 Nm^{-1}
Shaft diameter	10 mm	Stator stiffness (K_s)	1×10^7 Nm^{-1}
Disc inner-outer radius (R_r, R_s)	0.05-0.055 mm	Damper	200 ns/m
Friction coefficient (λ)	0.56	Restitution coefficient (ε)	0.7
Young modulus (E)	2.1×10^{11} N/m^2	Poisson ratio (v)	0.3
Fluid parameters (water)	Value and units	Mass (M)	16.845 kg
Fluid density (ρ_{fl})	1004 kg/m^3	Eccentricity mass ($m_{u*}e$)	0.003 kg·m
Fluid speed (Ω)	4.8522 rad/s	Motor moment of inertia (J_2)	0.36 kg·m^2
Amplitude ratio (X_0/l)	0.1666	Container width (l)	0.3 m
Fluid natural frequency (ω_{1n})	6.0084 rad/s	Disc moment of inertia (J_1)	0.1861 kg·m^2

(a)

(b)

(c)

(d)
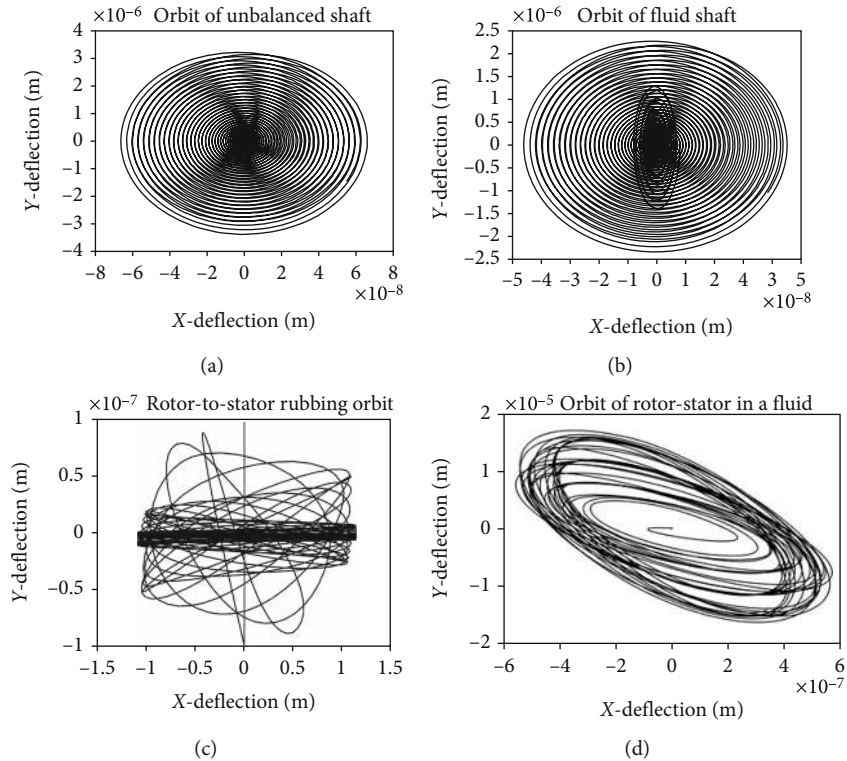
FIGURE 4: Orbits of the shaft in various conditions near the first critical speeds.

represents the influence of the hydrodynamic forces. The appearance of these harmonics is seen in the 3D NWSST plots (Figures 7(a) and 7(c)) which are attenuated in the presence of hydrodynamic forces. It can be noted that for a system in unbalance, a phase of the rise in instability around the equilibrium position (Figure 6(a)) and then a stabilization phase during which the amplitude of the movements continuously vary (Figures 6(a) and 6(b)). This established regime is also highlighted in Figure 4, where the convergence to a periodic orbit in the XY-displacement plane is perceived. The unbalance spectrum effect and the rotor-stator contact phenomenon can be established by the stored energy distribution of the higher frequencies observed in the marginal

spectra in Figure 8. However, there are some strong interference components, e.g., the multiple embraced part shown by a yellow line around the main frequency peak in Figures 8(c) and 8(d) which is excited by the frictional impact. Figures 8(a)–8(d) show that the rotor vibrations are periodic motions with sub- and superharmonics, which become quasiperiodic and regarded as chaos by some researchers, as stated in references [11, 12].

In Figure 8, a comprehensive examination of amplitude spectra shows that in specific points, the vibration level of the n-order harmonic reaches high values. This is the known sub- and superharmonic resonance phenomenon for nonlinear dynamic systems. From Figure 8(c) with shaft rotation,
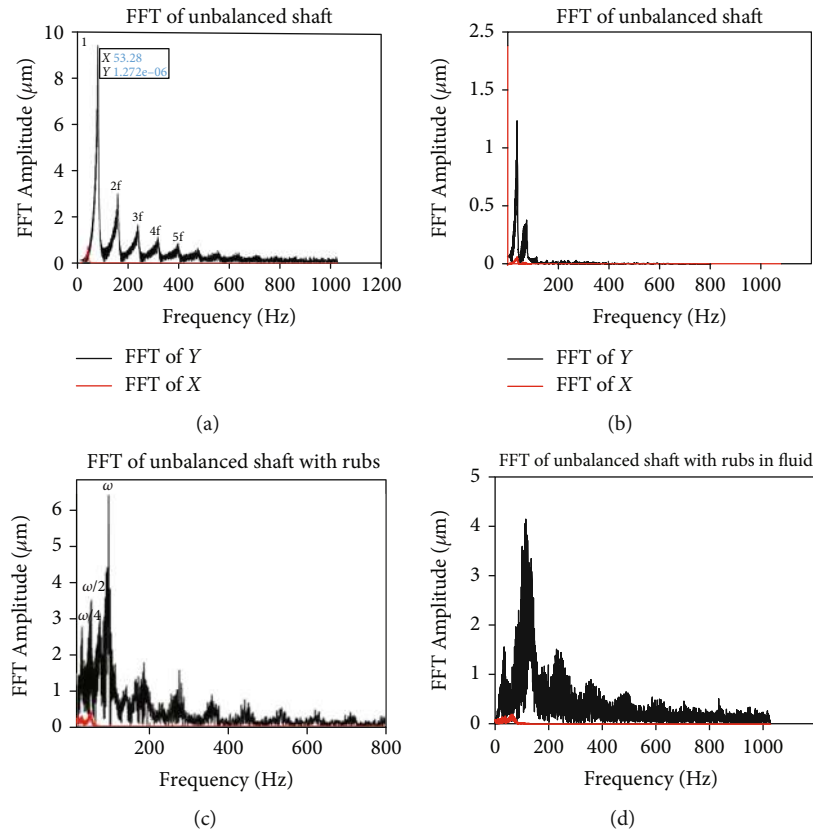
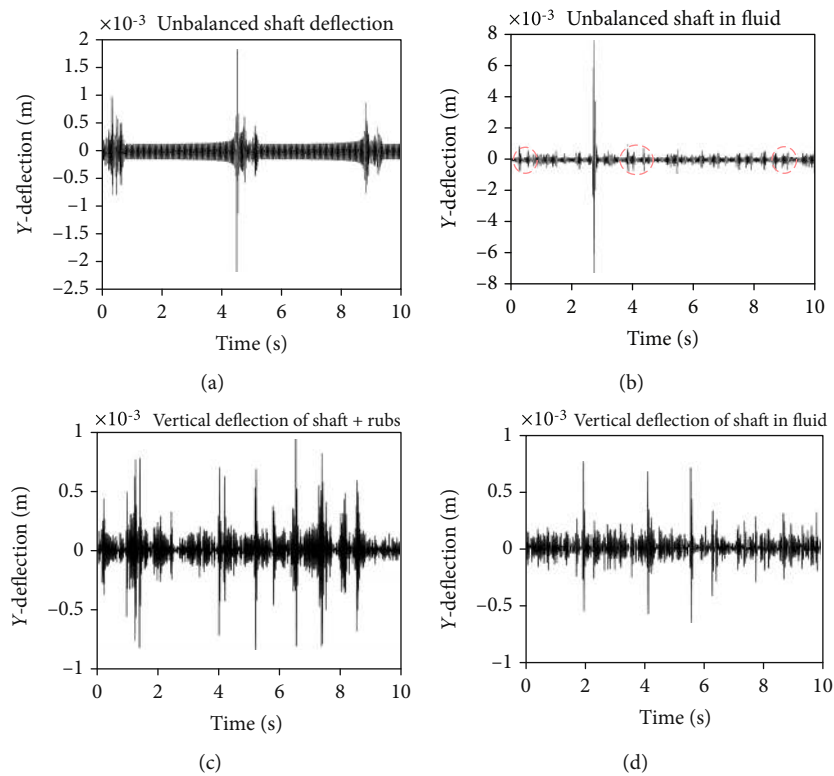Figure 5: FTT spectrum of the vibration response in the X and Y direction.

Figure 6: Vertical rotor deflection response with unbalance and rotor-to-stator rubbing.
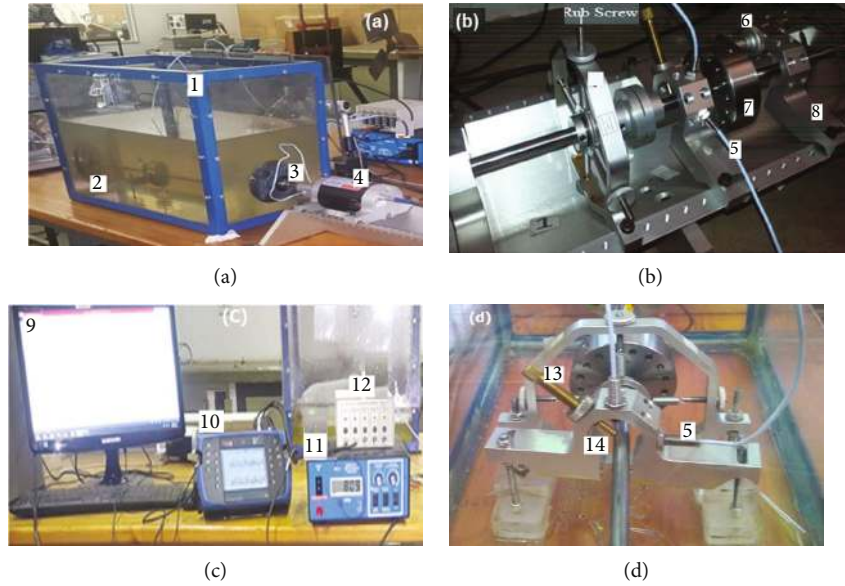
(a)

(b)

(c)

(d)

FIGURE 7: The experimental setup, rub screw setup, and data acquisition system.: 1—tank, 2—water, 3—flexible coupling, 4—motor, 5—probes, 6—mass unbalance, 7—disc, 8—rub housing, 9—computer screen, 10—scout-2013, 11—motor speed controller, 12—junction box, 13—rub screw, and 14—rotor-stator contact.
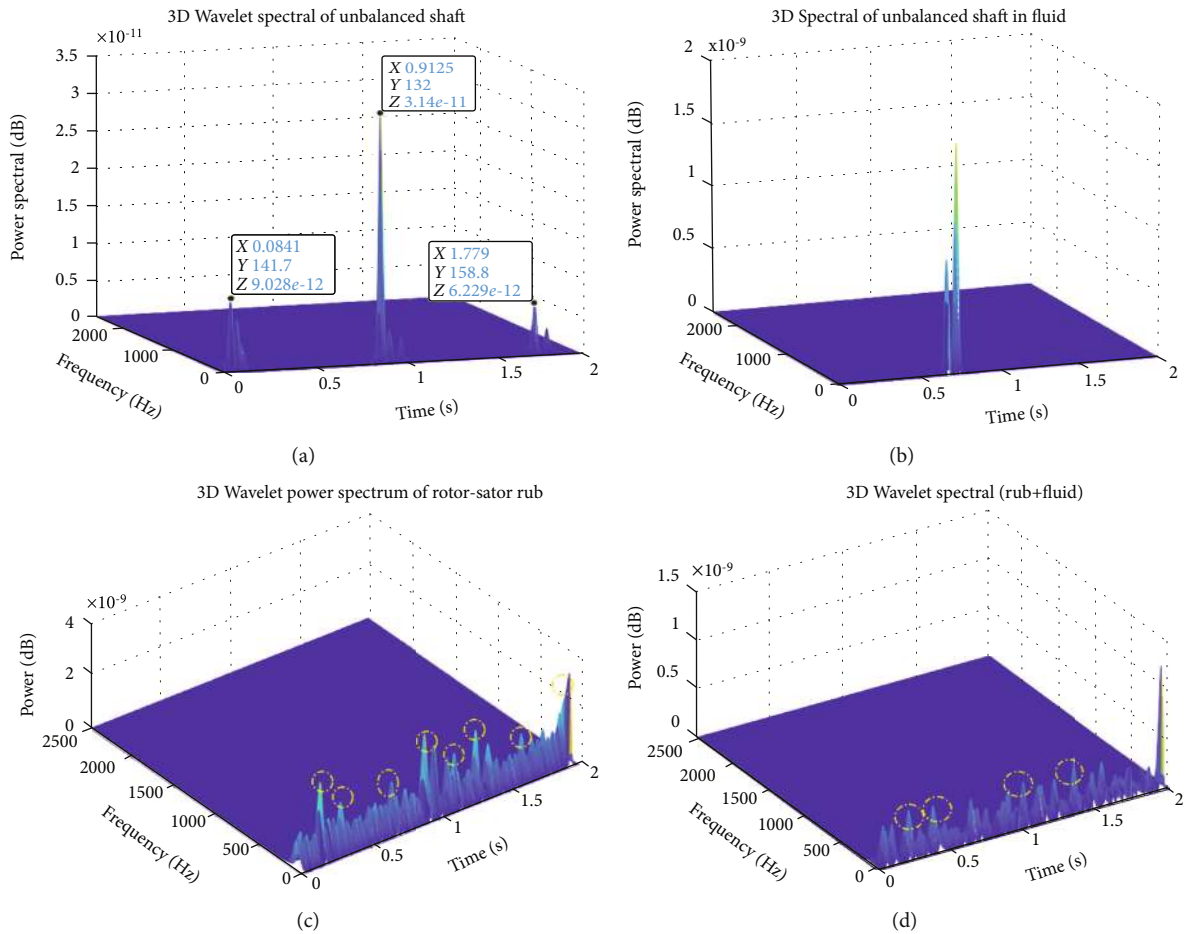

(a)

(b)

(c)

(d)

FIGURE 8: Corresponding 3D wavelet synchrosqueezing spectrum (NWSST) of the rotor system.

approximately quasiperiodical occurrences of the rub can roughly be observed. The NWSST spectral and the energy distributions from Figures 8(c) and 8(d) show that the rotor-stator contact phenomenon can be perceived despite the influences of the acting hydrodynamic forces. There are a few trivial harmonic interference components (e.g., the part embraced by the yellow dashed line in Figures 8(c) and 8(d)). Accumulated energy distribution of rubbing-impact can be observed from the marginal spectral in Figure 8(d). These higher frequencies disappear once the rotor interacts with the fluid. However, the mass of the fluid is found once again to affect the rubbing-impact with the periodic patterns of rotor vibrations. At the same time, dry friction leads to high quasiperiodical motions. This coincides in the characteristic extracted with the results obtained in Figures 6(c) and 6(d).

It can be noted that there are considerable mismatches on both frequency spectrum and time-frequency period of friction occurrences between the FFT (Figure 5(c)) and the NWSST (Figure 8(c)), due to the inherent drawbacks of energy distribution. These higher frequencies disappear as soon as rotor-stator rub occurs under the effects of fluid forces. Figure 8(b) shows a downward jump of frequency peak. The magnitude of the critical frequency and instability below and above the critical speed generated by rub fault are considerably reduced (Figure 8(b)) without oil lubricant. Since the rub-impact rotor system has a nonstationary and nonlinear nature, it is possible from NWSST energy to determine the precisely equal ranges of friction occurrence, which can facilitate feature extraction from the time-frequency. The above analysis shows that the presence of the fluid mass for dry contact reduces the vibration amplitude of the rotor system exponentially. The hydrodynamic forces also have the particularity of increasing the vibration of the system by generating some undesirable low and hidden harmony frequencies.

6. Experimental Setup and Empirical Approach

To validate the results of the theoretical model, an experimental setup has been developed using a modified Bently Nevada Rotor Kit 4. The test bench setup for the experiment is described in detail in the next section. The photograph presented in Figure 1 was designed and used for the analysis of the unbalance and rubbing-impact in a fluid medium. The experimental setup device consists of a rectangular tank, a flexible coupling used to connect the motor and the shaft. The rotating shaft with a length of 780 mm and a diameter of 10 mm is supported at each end by a reliable lubricated self-aligned bearing and carries a lumped mass disc. The entire test bench is mounted on a concrete block and isolated from the environment by a vibration absorber. The experimental devices permit the highlighting of vibratory phenomena, namely, the unbalance and rub excitations. The rotating system has been adjusted to reach up the maximum speed of 2500 rpm. To complete the assembly, the test bench includes six proximity transducers: four probes placed in vertical and horizontal directions at two specific positions (maximum vibration) are used to measure the vibration displacements of the rotor, its orbit patterns, and the frequency spectrum.

Four eddy current sensors connected to data acquisition device and two probe sensors are fixed at the vicinity of the rub location to measure the lateral displacements of the rotor in vertical and horizontal directions.

6.1. Experimental Procedure. The experimental test rig was performed on a modified Bently Nevada Rotor Kit 4. The data are collected using a set of Data Acquisition Interface Unit connected to the Ascent Vb7 device, which records the tachometer reading and displays the operational deflection shapes of the measured structures. A motor is installed to drive the rotor system, with the speed of the motor being controlled by a pulse width modulated which is dependent on the ramp up/ramp down switch (Figures 7(c) and 7(d)). The rated current of the electric motor is 2.5 A, and the output power is 250 W. The four proximity probes mounted at 90° right next to each shaft probes were coupled to a transducer unit powered by a DC power supply. Another proximity probe is located near the flexible coupling shaft to measure the rotational speed of the motor. The disc mass of 17 kg with 80 mm diameter and 25 mm thickness is connected at the midspan between the bearings, to neglect the gyroscopic effects of the disc. The shaft and disc are both made of steel (Young's modulus $E = 2.1011$ Pa, density $\rho = 7800$ kg/m^3). The discs that consist of twelve holes of diameter 10 mm with internal threads at a radial distance of 70 mm from the centre are provided for adding additional unbalance mass to the rotor (Figure 7(b)). The electric motor operated at a constant speed. As the shaft rotates in a filled tank, the tachometer laser is pointing directly on the shaft which comprises a fluorescent sticker capable of being detected by the laser. This sensor, therefore, captures the amplitude of the resonance. In order to avoid any irreversible deformation, the range of rotation frequencies is limited to the first bending frequency of the rotor. To better simulate the actual the rub-impact process, a design of a particular stator structure that allows a full rub experiment test to be performed was fabricated as shown in Figure 7(a). A rub-impact is established by adjusting a screw in the rub housing until the screw contacts the shaft. In this way, a rub screw holder is fixed at a specific position. Then, the electric motor was started to operate at the experimental speed. The contact is observed by threading the screw gradually downward until friction or knock is created. The desired degree of the rub is achieved by adjusting the screw and securing it in position with the locknut. The clearance between the rotor and the screw is adjustable to meet the experimental conditions. A transducer probe for measuring forces generated during friction was mounted near the contact point to combine the high sliding speed and high contact pressure. For the baseline result, the experiments were first performed with an unbalance mass at a maximum rotor kit operation speed of 1700 rpm; thus, the frequency of rotation is 28.328 Hz.

The sampling frequency is 1200 Hz, and the sampling points are 4096. The required unbalance was considered into the rotor system by adding in the disc shaft a trial mass of 34 gram at 0° plane. Experimental studies through various scenarios were therefore performed to focus on the relevant information in the orbit patterns, time displacement, and
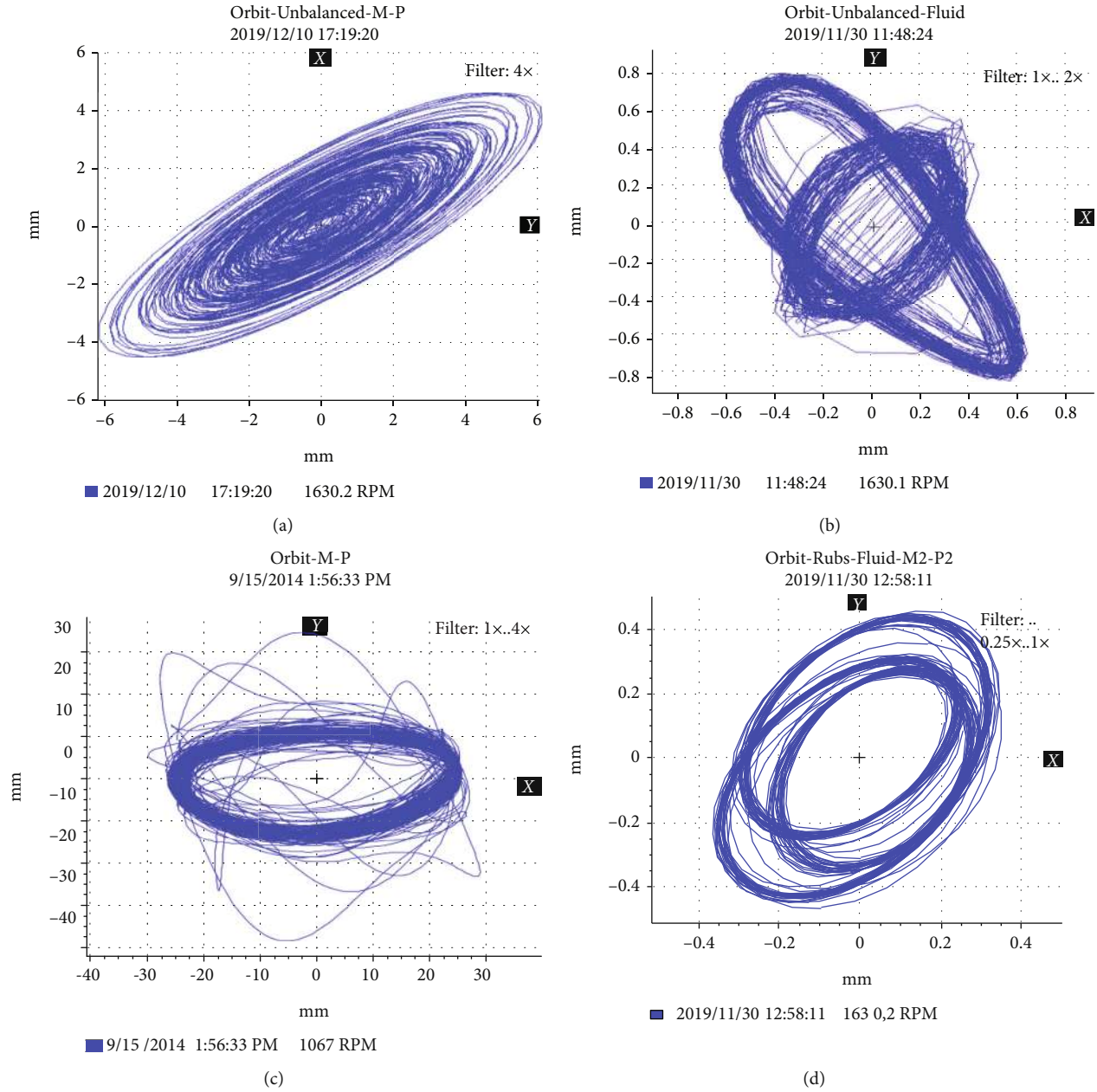
Figure 9: Orbits of the experimental shaft under rubbing conditions in air and fluid medium.

FFT spectrum and to discriminate the unbalance fault component. Initially, the experiment was carried out in an air medium with a rubbing impact. Then, the experiment was repeated inside the container (length $L = 700$ mm, height $h = 450$ mm, and width thickness $l_c = 400$ mm) with a filling volume of 70 litres, a shorter height with the same length and width. For the presented experiment, the rotor operates in air and fluid with an unbalanced mass which gradually leads to a rubbing contact excitation. The implementation of time-frequency is computationally done by importing the data signal efficiently from the data acquisition tools to the computer for analysis.

6.2. Experimental Result Discussion and Validation. The first experimental vibration signals from unbalanced rotor sys-

tems without and with rub-impact in air and water are processed, and the results in the form of orbits, waveform, and frequency spectrum are shown in Figures 9–11, respectively. The main peak values corresponding to the rotating frequency (73.75 Hz) can be easily observed in the air but at progressively low magnitude inside the fluid. According to Figures 9(a)–9(c) and the frequency spectrum in Figure 10(a), when rubbing-unbalance coupling fault occurs in air, the multiple frequencies and combination frequencies appear. The frequency spectrum of the system shown in Figure 10 indicates that a wide range of higher frequencies and many small peaks believed to be mainly caused by noise exist in the signal. The rub-impact is primarily consisting of abrupt, chaotic, and irregular bounces in orbit shapes; moreover, some inadequate and quasiperiodic rub-impact frequency appearance at high-
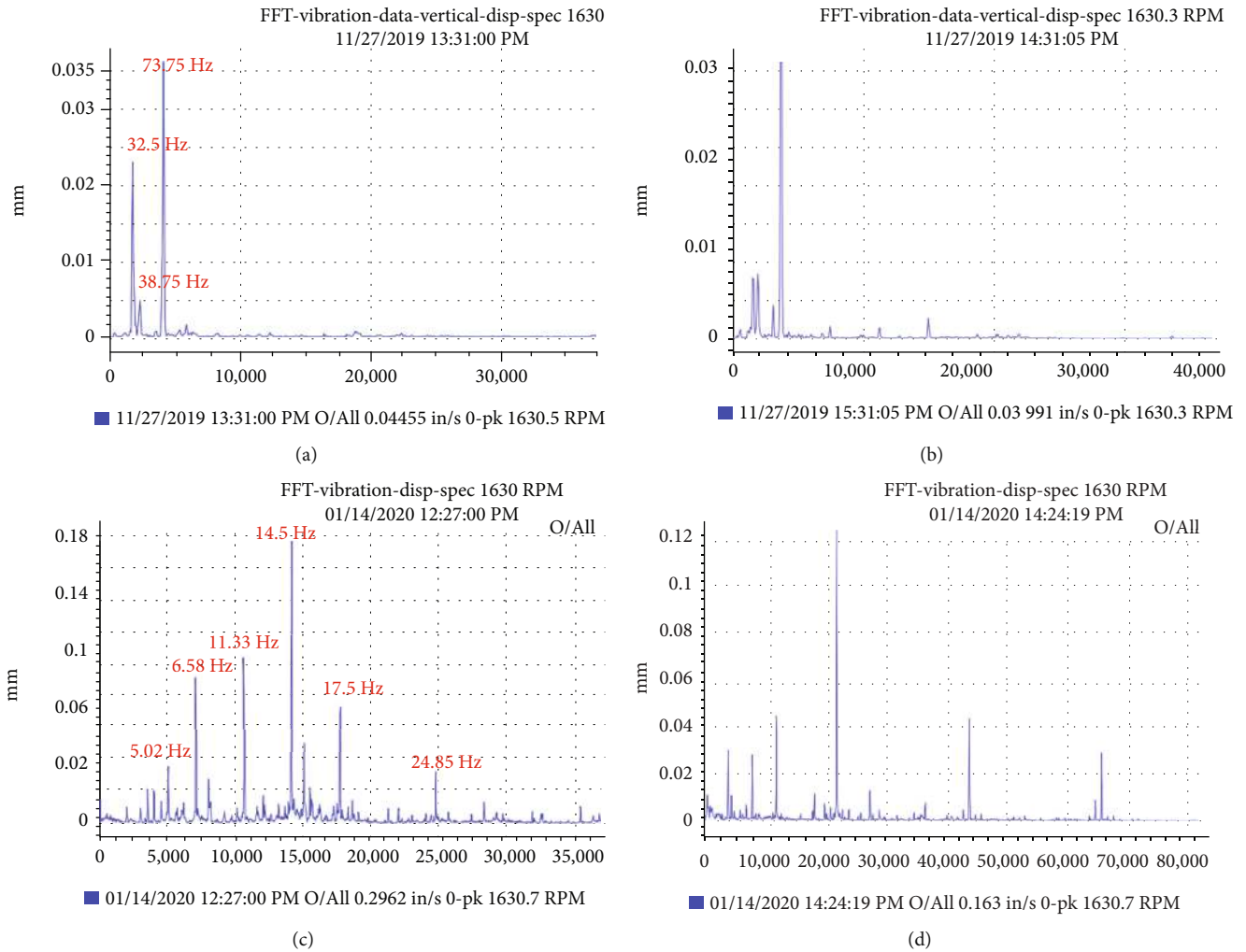
FIGURE 10: Experimental frequency spectrum of the unbalanced shaft under fluid-rubbing coupling conditions.

frequency occurs near the critical frequency 225.1 Hz. Figure 9(b) can reveal the feature nature of the rub vibrations, which was quite evident from their full spectra (refer Figures 10(b) and 11(b)).

The frequency components of the fluid-coupled rotor-stator are similar to the frequency components of rubbing fault in air; only the magnitude of the peak of frequencies is different (Figures 10(c) and 10(d)). The displacement in the Y-direction of the rubbing fault in the air is more prominent compared with that in the rubbing fault inside the fluid (Figures 11(c) and 11(d)). Due to the increase in rotation speed, the subharmonic rubbing vibration just occurs moderately in the region where the probability of rotor-stator contact is high under tight clearance conditions (Figures 12(a) and 12(b)). As the rotational speed of the unbalanced shaft becomes larger, synchronous vibration occurs in the region of the wide deflection range, as shown in Figures 10(a) and 11(a). The $1/n$ subharmonic vibration occurs from smaller unbalanced region, which is reduced drastically and regarded as a kind of medium-type vibration. As the integer n becomes more extensive, in the two environments where contact in fluid or not occurs, only the $1/n$ odd number subharmonic

peaks were informed of the presence of unbalance and rub-shocks, since the rotor orbit of the $1/n$ subharmonic vibrations informs about the rebound of the rotor from the origin of the point of contact. There are no significant features of rubbing on orbit-shape analysis to improve machine fault detection when the rotor was operating under the influence of fluid forces (see Figures 9(d) and 10(d)).

The time-frequency results of the experimental test conducted on rotor-stator rub in air and immersed into a tank are presented in Figure 12. In the presence of the rub-impact process without hydrodynamic force effects, the instantaneous frequency is quasiperiodical and increases sharply due to the impact effect (Figure 12(a)). The IF obtained by the NWSST is restrained to a lower level due to the stress resulting from resistive fluid forces (Figure 12(b)). The presence of fluid resistance forces can lead to the generation of another unforeseen excitation fault, for instance, higher vibration levels due to the coupling of an unbalanced rotor-stator rubbing surrounded by fluid in tight clearance situation. These two faults (rub and fluid forces) introduce nonlinearity to the rotor system, which generates higher subharmonics in the 3D NWSST response (in Figures 13(a) and
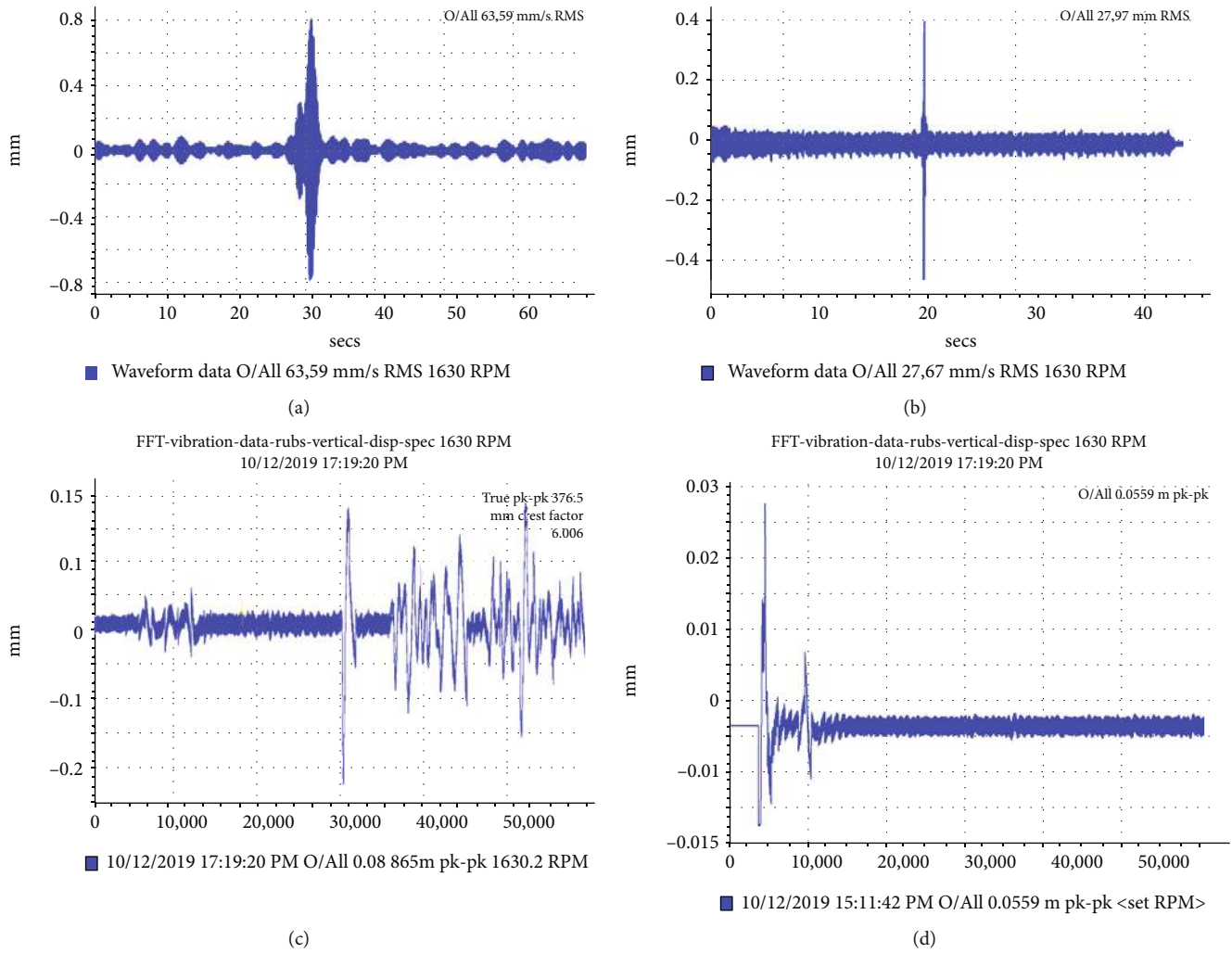
(a)

(b)

(c)

(d)

FIGURE 11: Experimental time history results of unbalanced rotor-to-stator rubbing under the fluid condition.
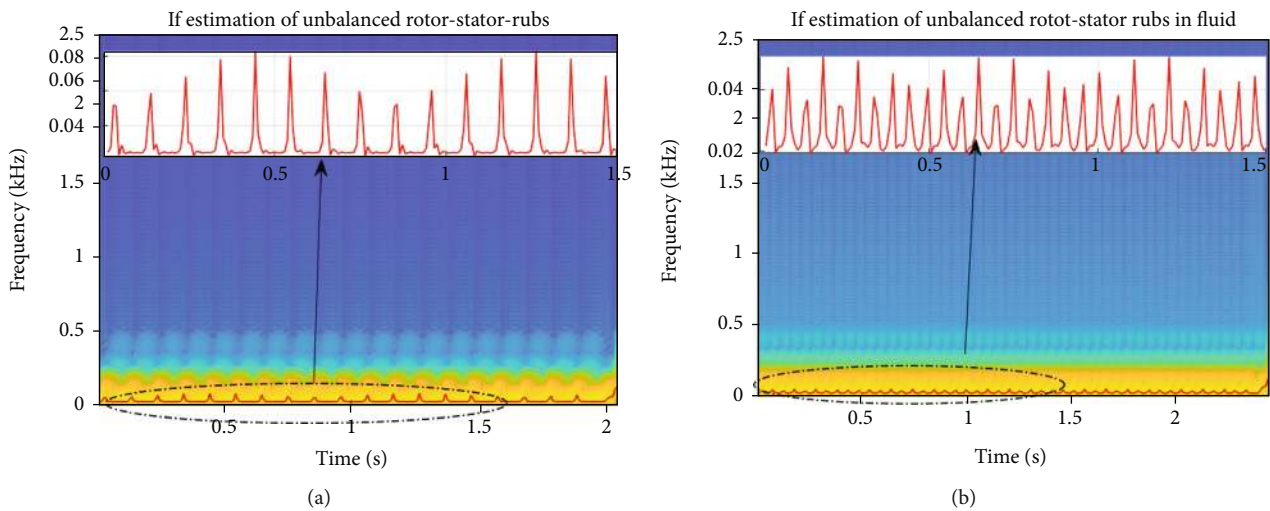

(a)

(b)

FIGURE 12: IF estimation of the dynamic response using the lateral rotor system. (a) In air and (b) fluid medium.
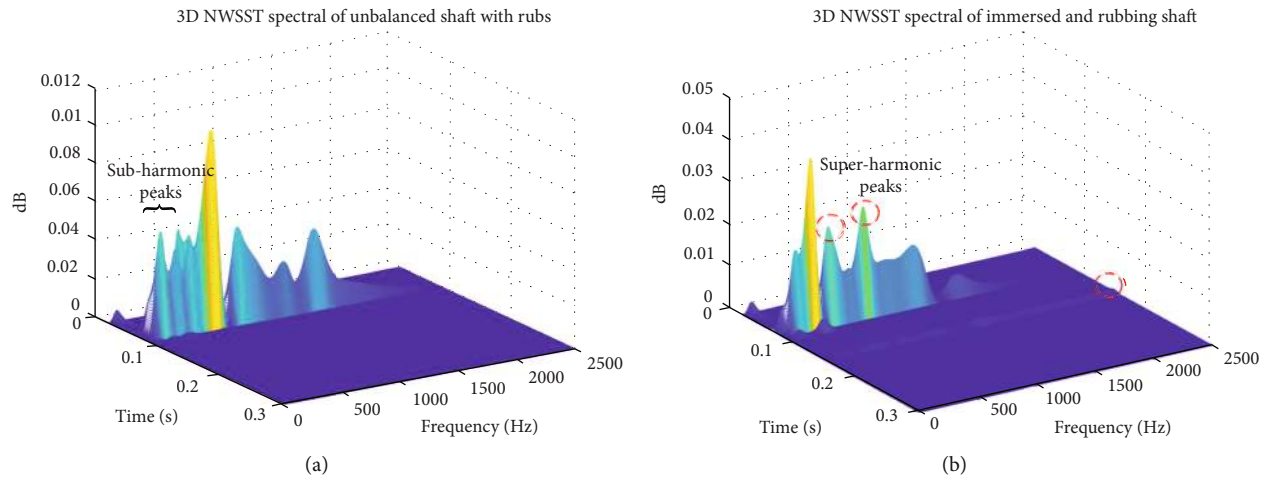
FIGURE 13: Experimental 3D Synchrosqueezing Spectrum results of the system (a) in air and (b) fluid medium.

13(b). Rotor-stator rub in a fluid generates few lower magnitudes of subharmonics in the 3D spectrum. Still, it exhibits significant and new supharmonics highlighted in red due to the effect of the fluid properties. For these observed frequencies in Figure 13(a), the first three harmonics are significant because they revealed the strong impact of disturbance when unbalance, rubbing impact, and fluid forces coexist in a rotor system. However, despite the effects of fluid, the 1× frequency still dominates the spectra at lower magnitude with or without fluid effects. This characteristic is typical to a rotor rub and can be used for rub diagnosis.

Finally, a comparison of the obtained experimental data with the simulation results showed good agreement for the damping factors of the inviscid fluid throughout the rubbing vibration behaviour in both media. The vibration signal deflection waveform of the rotor system with rubbing showed a severe rub-impact feature which significantly decreases in a filled container. It can be seen from the frequency spectrum that the signal mainly consists of vibrations caused by rub-impact and noise. However, in a fluid medium, the peak values are minimal and somewhere masked by the fluid properties. The comparison on the reproduced time history, orbit, and the full spectrum features of the rotating shaft measured by the experiment precisely at the contact point of one side of the screw impact and the simulation showed qualitatively the same trend as the previously reported papers [10–12]. The experimental results allow a deeper understanding of the underlying internal mechanisms of the fluid coupling to be achieved.

7. Conclusion

This paper proposed a coupled fluid-rotor interaction model to analyse the influences of hydrodynamic forces on the rotor-stator-rubbing defect in rotating machine by numerical and experimental methods. The governing equations of the system corresponding to one rotation and two lateral deflections of a horizontal rotor-stator system partially immersed in a fluid medium are established. The model takes into account the eccentric mass, the parametric excitation induced by the rotor-stator rub, and the hydrodynamic forces, resulting in a highly nonlinear system. The methods of controlling the rotor-stator vibration, including the interaction of the inviscid fluid with the rotor system under operational conditions, are validated in various scenarios. The conclusions drawn from the study can be summarized as follows:

(1) The numerical and experimental results confirm that the contact noise and greater amplitude of the rubbing-impact vibration can be effectively reduced by introducing the hydrodynamic forces into the system

(2) In practice, the response orbits of the system clearly show the rotor-to-stator impact contact in the event of severe rub-impact. The low- and weak-frequency components having periodically abrupt fluctuations are observed with significant differences between rub-impact in air and fluid medium

(3) The extracted IF's and the dissipative energy of the system in contact using a synchrosqueezing wavelet transform technique has shown that the impact of the rotor on the fixed stator in the fluid medium generates considerable subharmonics at low magnitudes and also exhibited some undesirable and unexpected new superharmonics due to the effect of fluid fluctuation and noise at the contact point

(4) Numerical and experimental results have shown that the amplitude of vibration signal decreases by more than 25% in fluid medium but with some higher IF's fluctuation which can be a good indicator of rubbing effects in an inviscid fluid

Finally, this work opens the debate on the hypotheses to be made concerning the lubricant. As usually envisaged in many mechanical systems, partially adding damping could not always be the effective tool to fight against strong vibrational phenomena as the properties of the fluid influence the phenomenon of contact of the system described by generating an unwanted increase in the amplitude of vibrations.

Data Availability

The data used to support the findings of this study are included within the article.

Conflicts of Interest

The authors declare that they have no known competing for financial interests or personal relationships that could have appeared to influence the work reported in this paper.

Acknowledgments

References

[1] H. J. P. Morand and R. Ohayon, *Fluid-structure interaction-applied numerical methods*, Wiley, 1995.

[2] Y. Bazilevs, K. Takizawa, and T. E. Tezduyar, *Computational Fluid-Structure Interaction: Methods and Applications*, John Wiley & Sons, 2013.

[3] S. G. Kadyrov, J. Wauer, and S. V. Sorokin, "A potential technique in the theory of interaction between a structure and a viscous, compressible fluid," *Archive of Applied Mechanics*, vol. 71, no. 6-7, pp. 405–417, 2001.

[4] A. Kydyrbekuly, L. Khajiyeva, A. Y. Gulama-Garyp, and J. Kaplunov, "Nonlinear vibrations of a rotor-fluid-foundation system supported by rolling bearings," *Strojniski Vestnik/Journal of Mechanical Engineering*, vol. 62, no. 6, 2016.

[5] B. X. Tchomeni and A. A. Alugongo, "Modelling and numerical simulation of vibrations induced by mixed faults of a rotor system immersed in an incompressible viscous fluid," *Advances in Mechanical Engineering*, vol. 10, no. 12, 2018.

[6] J. P. Gomes and H. Lienhart, "Fluid-structure interaction-induced oscillation of flexible structures in laminar and turbulent flows," *Journal of Fluid Mechanics*, vol. 715, pp. 537–572, 2013.

[7] L. Xiang, A. Hu, L. Hou, Y. Xiong, and J. Xing, "Nonlinear coupled dynamics of an asymmetric double-disc rotor-bearing system under rub-impact and oil-film forces," *Applied Mathematical Modelling*, vol. 40, no. 7-8, pp. 4505–4523, 2016.

[8] S. Popprath and H. Ecker, "Nonlinear dynamics of a rotor contacting an elastically suspended stator," *Journal of Sound and Vibration*, vol. 308, no. 3-5, pp. 767–784, 2007.

[9] N. Bachschmid, P. Pennacchi, and A. Vania, "Thermally induced vibrations due to rub in real rotors," *Journal of Sound and Vibration*, vol. 299, no. 4-5, pp. 683–719, 2007.

[10] L. Banakh and L. Nikiforov, "Vibroimpact regimes and stability of system "rotor—sealing ring"," *Journal of sound and vibration*, vol. 308, no. 3-5, pp. 785–793, 2007.

[11] R. Zhu, G. C. Wang, Q. P. Han, A. L. Zhao, J. X. Ren, and X. Xia, "Dynamic characteristics and experimental research of a two-span rotor-bearing system with rub-impact fault," *Shock and Vibration*, vol. 2019, 15 pages, 2019.

[12] J. A. N. Hengstler, *Influence of the Fluid-Structure Interaction on the Vibrations of Structures*, ETH Zurich, Zurich, 2013.

[13] A. Presas, E. Egusquiza, C. Valero, D. Valentin, and U. Seidel, "Feasibility of using PZT actuators to study the dynamic behavior of a rotating disk due to rotor-stator interaction," *Sensors*, vol. 14, no. 7, pp. 11919–11942, 2014.

[14] S. Lahriri, H. I. Weber, I. F. Santos, and H. Hartmann, "Rotor–stator contact dynamics using a non-ideal drive-theoretical and experimental aspects," *Journal of Sound and Vibration*, vol. 331, no. 20, pp. 4518–4536, 2012.

[15] R. A. Ibrahim, "Liquid Sloshing Dynamics," in *Theory and Applications*, Cambridge University Press, 2005.

[16] S. Wang, X. Chen, Y. Wang, and B. Ding, "Nonlinear squeezing transform for weak signal detection, Signal and Information Processing," in *IEEE China Summit & International Conference on*, pp. 718–722, Xi'an, China, 2014.

[17] I. G. Thakur, E. Brevdo, N. S. Fučkar, and H. T. Wu, "The Synchrosqueezing algorithm for time-varying spectral analysis: robustness properties and new paleoclimate applications," *Signal Processing*, vol. 93, no. 5, pp. 1079–1094, 2013.